

SLOW RISE AND PARTIAL ERUPTION OF A DOUBLE-DECKER FILAMENT. I OBSERVATIONS AND INTERPRETATION

RUI LIU^{1,2}, BERNHARD KLIEM^{3,4}, TIBOR TÖRÖK⁵, CHANG LIU², VIACHESLAV S. TITOV⁵,
ROBERTO LIONELLO⁵, JON A. LINKER⁵, AND HAIMIN WANG^{2,6}

Draft version August 16, 2012

ABSTRACT

We study an active-region dextral filament which was composed of two branches separated in height by about 13 Mm, as inferred from three-dimensional reconstruction by combining *SDO* and *STEREO-B* observations. This “double-decker” configuration sustained for days before the upper branch erupted with a *GOES*-class M1.0 flare on 2010 August 7. Analyzing this evolution, we obtain the following main results. 1) During hours before the eruption, filament threads within the lower branch were observed to intermittently brighten up, lift upward, and then merge with the upper branch. The merging process contributed magnetic flux and current to the upper branch, resulting in its quasi-static ascent. 2) This transfer might serve as the key mechanism for the upper branch to lose equilibrium by reaching the limiting flux that can be stably held down by the overlying field or by reaching the threshold of the torus instability. 3) The erupting branch first straightened from a reverse S shape that followed the polarity inversion line and then writhed into a forward S shape. This shows a transfer of left-handed helicity in a sequence of writhe-twist-writhe. The fact that the initial writhe is converted into the twist of the flux rope excludes the helical kink instability as the trigger process of the eruption, but supports the occurrence of the instability in the main phase, which is indeed indicated by the very strong writhing motion. 4) A hard X-ray sigmoid, likely of coronal origin, formed in the gap between the two original filament branches in the impulsive phase of the associated flare. This supports a model of transient sigmoids forming in the vertical flare current sheet. 5) Left-handed magnetic helicity is inferred for both branches of the dextral filament. 6) Two types of force-free magnetic configurations are compatible with the data, a double flux rope equilibrium and a single flux rope situated above a loop arcade.

Subject headings: Sun: filaments, prominences—Sun: flares—Sun: coronal mass ejections (CMEs)

1. INTRODUCTION

It is generally accepted that the magnetic field plays a crucial role for dense and cold filaments to be suspended in and thermally isolated from the surrounding hot, tenuous coronal plasma. Filaments are always formed along a polarity inversion line (PIL) of the photospheric field. Studies utilizing Zeeman and Hanle effects demonstrated that the flux threading the filament is largely horizontal and mainly directed along the filament axis (Leroy 1989; Bommier et al. 1994). This is also manifested in the chromospheric fibril pattern (Martin 1998, and references therein): fibrils near the filament are nearly parallel to the filament axis, but away from the filament they tend to be perpendicular to the filament axis. This pattern implies the presence of two types of *filament chirality*: for an observer viewing the filament from the positive-polarity side, the axial field in a *dextral* (*sinistral*) filament always points to the right (left). Independent of the solar cycle, dextral (*sinistral*) filaments are predominant in the northern (southern) hemisphere (Martin et al. 1994; Zirker et al. 1997;

Pevtsov et al. 2003).

Most quiescent filaments have what is known as *inverse polarity* configuration, i.e., the magnetic field component perpendicular to the axis traverses the filament from the region of negative polarity to the region of positive polarity in the photosphere, opposite to what would be expected from a potential field. *Normal polarity* configuration is mainly found in active-region filaments, i.e., the field lines pass through the filament from the region of positive polarity to the region of negative polarity (Leroy 1989). Magnetic configurations with either a dipped field or a helically coiled field have been invoked to explain the equilibrium and stability of filaments, which leads to three basic filament models as reviewed by Gilbert et al. (2001): the normal polarity dip model (e.g., Kippenhahn & Schlüter 1957), the normal polarity flux rope model (e.g., Hirayama 1985; Leroy 1989), and the inverse polarity flux rope model (e.g., Kuperus & Raadu 1974; Pneuman 1983; Anzer 1989; Low & Hundhausen 1995). In addition, by transporting the core flux into regions of increasingly weak field via shear flows, Antiochos et al. (1994) were able to produce a dipped, inverse-polarity configuration of sheared field lines. By applying greater shear, DeVore & Antiochos (2000) find that magnetic reconnection produces helical field lines threading the filament. In all these models, the magnetic tension force pointing upward provides mechanical support for the filament material against gravity. Alternatively, Karpen et al. (2001) found that cool plasma can be supported in a dynamic state on flat-topped arcade field lines and argued that magnetic dips are not necessary for the formation and suspension of filaments.

The correspondence between the filament chirality and

rliu@ustc.edu.cn

¹ CAS Key Laboratory of Geospace Environment, Department of Geophysics & Planetary Sciences, University of Science & Technology of China, Hefei 230026, China

² Space Weather Research Laboratory, Center for Solar-Terrestrial Research, NJIT, Newark, NJ 07102, USA

³ Institute of Physics and Astronomy, University of Potsdam, 14476 Potsdam, Germany

⁴ Mullard Space Science Laboratory, University College London, Holmbury St. Mary, Dorking, Surrey RH5 6NT, UK

⁵ Predictive Science Inc., 9990 Mesa Rim Road, Suite 170, San Diego, CA 92121, USA

⁶ Key Laboratory of Solar Activity, National Astronomical Observatories, Beijing, China

the helicity sign has been controversial due to different opinions on how the filament is magnetically structured. Rust (1994) conjectured that sinistral (dextral) filaments are threaded by right-handed (left-handed) helical fields, considering that barbs, which are lateral extensions veering away from the filament spine, should rest at the bottom of the helix. Martin & Echols (1994), on the other hand, noticed that the ends of barbs are fixed at patches of parasitic polarities (also termed minority polarities), which are opposite in polarity to the network elements of majority polarity, and suggested that dextral filaments are right-helical. Chae et al. (2005), however, reported that the barbs terminate over the minority-polarity inversion line. This lends support to the suggestion that the barb material is suspended in field line dips which form due to the existence of parasitic polarities. The latter scenario is consistent with force-free field models (Aulanier & Démoulin 1998; Aulanier et al. 1998), in which the filament spine, the barbs, and the surrounding fibrils are all modeled as the dipped portions of the field lines. With projection effects, a continuous pattern of dipped field lines could give the illusion that barbs are made of vertical fields joining the spine to the photosphere. Projection effects also contribute to the confusion about the chirality-helicity correspondence of the sigmoidal structures in the corona: the projection of a single twisted field line includes both forward and inverse S-shapes (Gibson et al. 2006). Furthermore, a left-handed flux rope can take either forward or reverse S-shapes depending on whether it kinks upward or downward (Kliem et al. 2004; Török et al. 2010).

Considerable attention has been given to the eruption of filaments, with the dense filament material tracing the otherwise invisible progenitor of the coronal mass ejection (CME). Relevant models can be roughly classified into two categories: those that rely on magnetic reconnections to remove the tethering field so that the filament can escape (Moore et al. 2001; Antiochos et al. 1999); and those in which the eruption occurs when a flux rope loses equilibrium, due to a catastrophe (e.g., van Tend & Kuperus 1978; Forbes & Priest 1995) or due to ideal MHD instabilities (e.g., Hood & Priest 1979; Kliem & Török 2006). While the torus instability almost certainly plays a role (Liu 2008; Aulanier et al. 2010; Fan 2010), the occurrence of the helical kink mode has recently been quite controversial. It is motivated by observations of writhed eruptive structures (e.g., Rust & Kumar 1994, 1996; Ji et al. 2003; Romano et al. 2003; Rust & LaBonte 2005; Alexander et al. 2006; Liu et al. 2007c; Liu & Alexander 2009; Cho et al. 2009; Karlický & Kliem 2010), most of which are filaments. It is also supported by successful MHD numerical modeling of key properties of eruptions, e.g., writhe, rise profile, and sigmoidal features, and of specific eruptive events (e.g., Fan & Gibson 2004; Fan 2005, 2010; Gibson & Fan 2006b; Török et al. 2004; Török & Kliem 2005; Kliem et al. 2010). On the other hand, signatures of the required amount of twist prior to the eruption remain difficult to detect (e.g., Chae 2000; Su et al. 2011). Eruptions driven by the kink instability also provide an opportunity to determine the helicity sign of the filament. Due to helicity conservation, an unstable flux rope only writhes into a kink of the same handedness, which can be inferred from the writhing motion of the filament axis (e.g., Green et al. 2007), especially if stereoscopic observations are available.

In this paper we address these issues in analyzing the observations of an eruptive filament which showed strong writhing

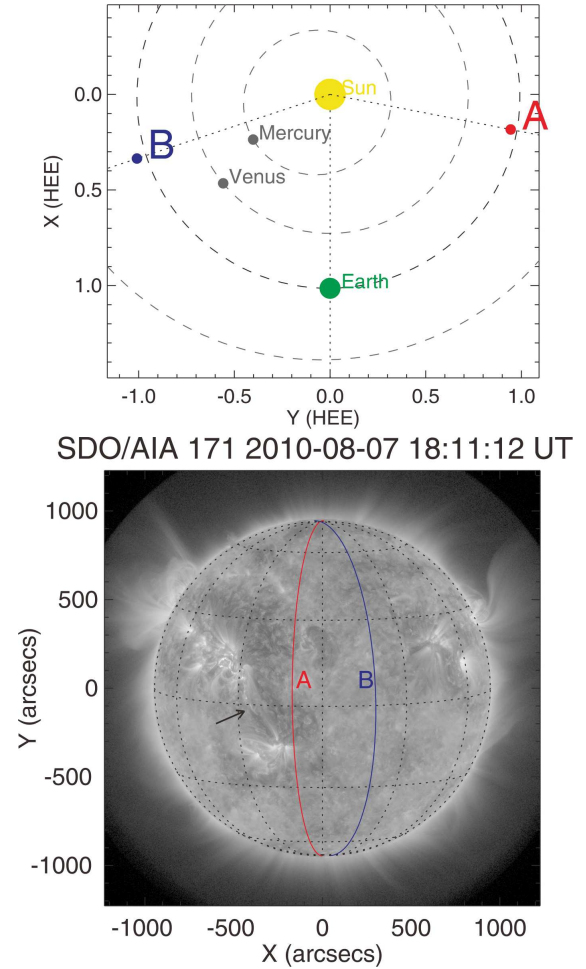


FIG. 1.— *Top*: positions of the pair of *STEREO* satellites in the Heliocentric Earth Ecliptic (HEE) coordinate system at about 18:00 UT on 2010 August 7; *Bottom*: red and blue curves indicate the limb positions of the *STEREO* “Ahead” and “Behind” satellites, respectively, on an *SDO* image taken near the onset of the eruption. The arrow marks a group of transequatorial loops connecting AR 11093 in the northern hemisphere, where a sigmoid is visible, and AR 11095 in the south.

motions preceded by unwrithing motions. The filament had a special “double-decker” configuration and formed a hard X-ray (HXR) sigmoidal source of coronal origin between the rapidly rising upper branch and the stable lower branch, which provides some unique insight into the physics of solar filaments and their eruption. The observations and data analysis are presented in Section 2. Interpretations are discussed in Section 3. Section 4 summarizes the main results.

In Paper II (Kliem et al. 2012b) we consider the existence, stability, and instability of equilibria containing two vertically arranged force-free flux ropes in bipolar external field, which further corroborates our interpretations based on the present data analysis and suggests new models for partial eruptions.

2. OBSERVATIONS AND DATA ANALYSIS

2.1. Instruments and Data Sets

The key data sources in this study include the EUV imaging instruments onboard the *Solar Dynamic Observatory* (*SDO*) and the *Solar Terrestrial Relations Observatory* (*STEREO*; Kaiser et al. 2008), and the *Reuven Ramaty High Energy Solar Spectroscopic Imager* (*RHESSI*; Lin et al. 2002).

The Atmospheric Imaging Assembly (AIA; Lemen et al.

2011) onboard *SDO* takes EUV/UV images at multiple wavelengths with a resolution of $\sim 1''.2$ and a cadence of 12 seconds for each individual wavelength, covering an unprecedentedly wide and nearly continuous temperature range. AIA Level-1 data are further processed using the standard SSW procedure AIA_PREP to perform image registration.

The Extreme-UltraViolet Imager (EUVI; Wuelser et al. 2004) of the Sun Earth Connection Coronal and Heliospheric Investigation (SECCHI; Howard et al. 2008) imaging package onboard both *STEREO* satellites provides three passbands, namely, 171 Å (Fe IX), 195 Å (Fe XII) and 304 Å (He II). The top panel of Figure 1 shows the positions of the *STEREO* “Ahead” and “Behind” satellites (hereafter referred to as *STEREO-A* and *STEREO-B*, respectively) in the X-Y plane of the Heliocentric Earth Ecliptic (HEE) coordinate system. In the bottom panel, the red and blue arcs mark the corresponding limb positions of the *STEREO* satellites in the AIA image obtained at 18:11 UT on 2010 August 7. The active region of interest, NOAA Active Region 11093, was located at N12E31, connecting with AR 11095 (S19E20) in the southern hemisphere through a group of transequatorial loops as indicated by an arrow.

2.2. Pre-eruption Configuration

The filament located in AR 11093 was composed of two branches, hereafter referred to as the *lower branch* and the *upper branch*. As shown in Figure 2, the lower branch was aligned along the PIL as filaments usually do, while the upper branch was projected onto the region of positive polarities, owing to the fact that it was located high in the corona (Section 2.3). The southern ends of both branches were apparently rooted in the penumbra of the sunspot that was of negative polarity. (Note that due to the projection effect the field in the eastern periphery of the penumbra possessed a positive component along the line of sight. This is clearly demonstrated in the line-of-sight magnetogram taken two days later (bottom panel of Figure 2), in which the sunspot was close to the disk center and the positive patch to the east of the sunspot has disappeared.) Hence, the field direction along the filament axis must be pointing southward, spiraling counterclockwise into the sunspot. Therefore, both branches of the filament were dextral, according to the definition of the filament chirality (Martin 1998). This is consistent with the empirical hemispheric chirality rule of filaments.

2.3. 3D Reconstruction and Analysis

By using a pair of EUV images taken from different perspectives, the three-dimensional location of the filament under investigation can be derived by a triangulation technique called *tie point* (Inhester 2006). This is implemented in an SSW routine, SCC_MEASURE, by W. Thompson and has been utilized to obtain the three-dimensional shape and height of filaments observed by *STEREO* (e.g., Li et al. 2010; Xu et al. 2010; Seaton et al. 2011; Bemporad et al. 2011; Thompson et al. 2012). In our case, *STEREO-B* images are to be paired with earth-view images provided by *SDO*, as the filament was occulted from the *STEREO-A* view (Figure 1). In EUVI images, the filament is more clearly defined with better contrast in 171 Å than in 195 Å or 304 Å, but 171 Å images are often not available, suffering from much lower cadence (2 h) than the other two channels (usually 5–10 min).

The two observers, *SDO* and *STEREO-B*, and the point in the solar corona to be triangulated define a plane called the

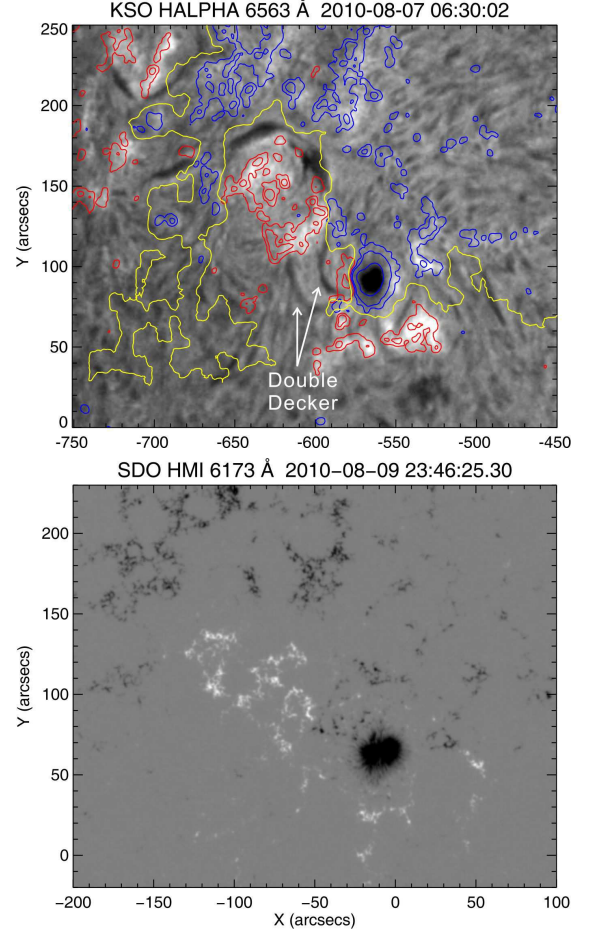


FIG. 2.— $H\alpha$ image taken by Kanzelhöhe Solar Observatory (KSO; top panel), overlaid by an HMI line-of-sight magnetogram taken at the same time. Contour levels indicate the magnitude of magnetic flux density at 50, 200, and 800 G for positive (red) and negative (blue) polarities. Yellow contours indicate the major PIL of the active region. The bottom panel shows a line-of-sight magnetogram taken two days later when the sunspot was close to the disk center.

epipolar plane. For each observer, the epipolar plane intersects with the image plane in the epipolar line. The basis for triangulation is known as the epipolar constraint (Inhester 2006), i.e., a point identified on a certain epipolar line in one image must be situated on the corresponding epipolar line in the other image. Matching features that appear on a pair of epipolar lines therefore establishes a correspondence between pixels in each image, and the reconstruction is achieved by tracking back the lines of sight for each pixel, whose intersection in the same epipolar plane defines a unique location in three-dimensional space.

Figure 3 shows two pairs of EUV images from AIA onboard *SDO* and from EUVI onboard *STEREO-B* taken on 2010 August 5 and 7. On August 5, both branches of the filament can be clearly seen in the AIA image (Figure 3(b)), while only a single thread-like structure of reverse S-shape was displayed by the corresponding *STEREO-B* image (Figure 3(a)). For *STEREO-B* the filament was located close to the disk center, suggesting that the upper branch was located right above the lower branch. Hence, we will refer to the configuration as a “double-decker filament.” By triangulation, we obtain the height of the upper branch, which was at about 30 ± 3 Mm above the solar surface. The reconstruction error is $\sim w/\sin \alpha \simeq 2.6$ Mm, where $w \simeq 2.5$ Mm is the width

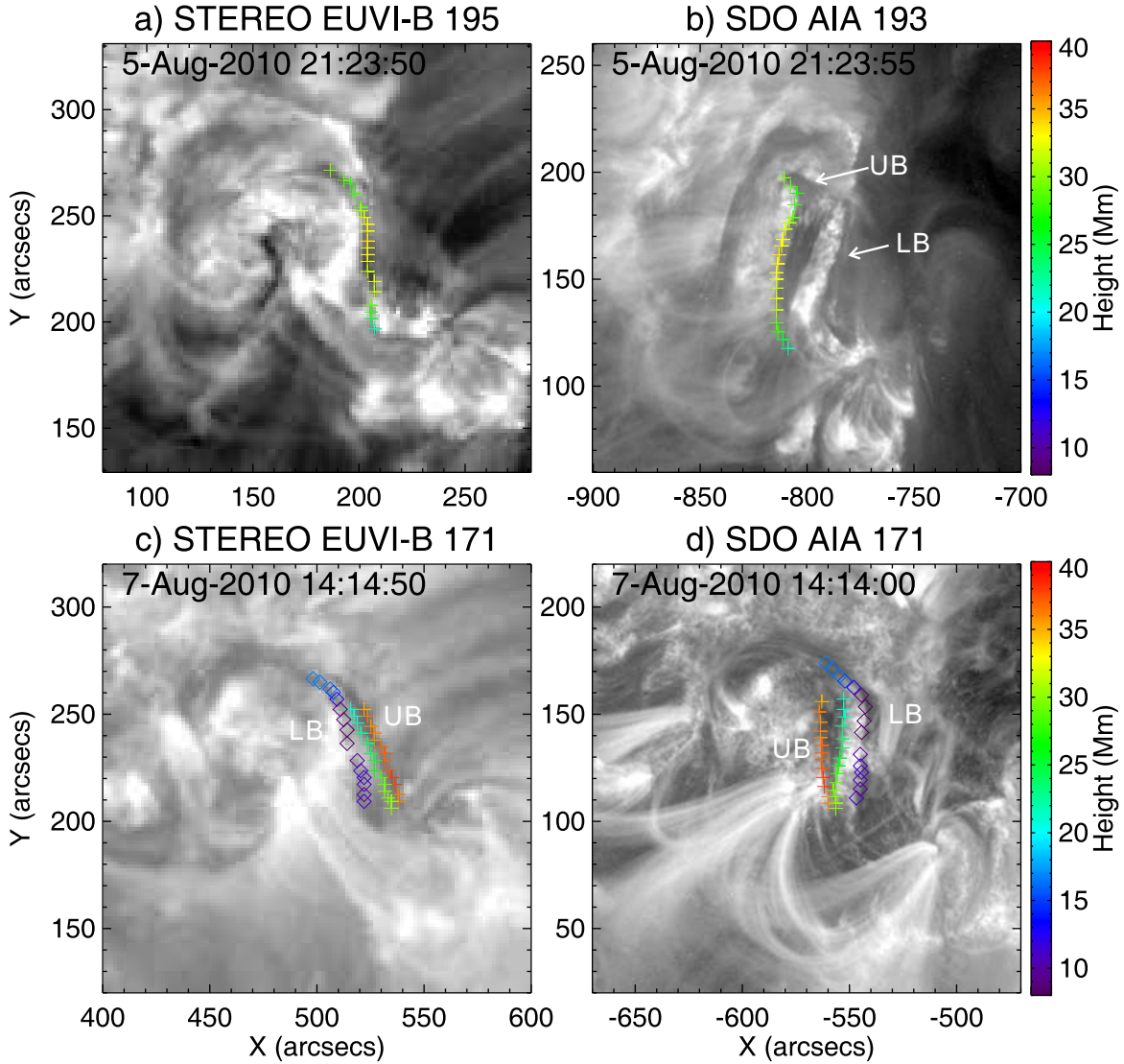


FIG. 3.— Three-dimensional reconstruction of the filament height using the tie-point method. Points on the upper branch (UB) are indicated by crosses and those on the lower branch (LB) by diamonds. The heights of these points above the solar surface in Mm are color-coded as indicated by the color bar on the right.

of the observed filament thread in the *STEREO-B* image and $\alpha \simeq 71^\circ$ is the separation angle between *STEREO-B* and *SDO* on August 5.

On August 7, the two branches were visible in both the *STEREO-B* and *SDO* views (Figure 3(c) and (d)). About 4 hours later, the upper branch in the *SDO* view moved eastward and then erupted, while in the *STEREO-B* images, one can see that the branch in the west moved westward and then erupted. Hence we are able to match the two branches unambiguously in the image pair, Figure 3(c) and (d). For the upper branch, the triangulation results show that its upper rim was located at about 36 ± 2 Mm above the surface, 6 Mm higher than it was on August 5, corresponding to an average rising speed of about 0.1 km s^{-1} . Its lower rim was 25 ± 3 Mm high, hence the vertical extent of the upper branch was about 11 ± 4 Mm. For the lower branch, its upper rim had a height of about 12 ± 3 Mm, which was separated from the lower rim of the upper branch by a distance similar to the vertical extension of the upper branch.

2.4. Filament Rise and Eruption

The evolution of the active region's photospheric field in the course of the 1–2 days during which it was well visible before the eruption was mainly characterized by the moat flow around the sunspot and ongoing gradual dispersion of the positive polarity flux in the northern hook of the filament. Episodes of significant new flux emergence, shearing, or cancellation were not observed. Weak flux cancellation proceeded at the north-south directed section of the PIL under the middle of the filament. The two filament branches did not show strong changes in position either. However, there were quite dramatic signs of interaction between them, which appeared to be the most significant changes associated with the filament system, in addition to the weak flux cancellation under its middle part. Episodes repeatedly occurred in which a dark thread within the lower branch was heated, brightened, lifted upward, and merged with the upper branch, apparently cooling down again. To show this evolution, we place a virtual “slit” across the center of the double-decker filament in the AIA 304 Å images and generate a stack plot from these data. The slit is taken to be 260 by 10 pixels spanning from $-719.7''$ to $-564.3''$ in the east-west direction and from

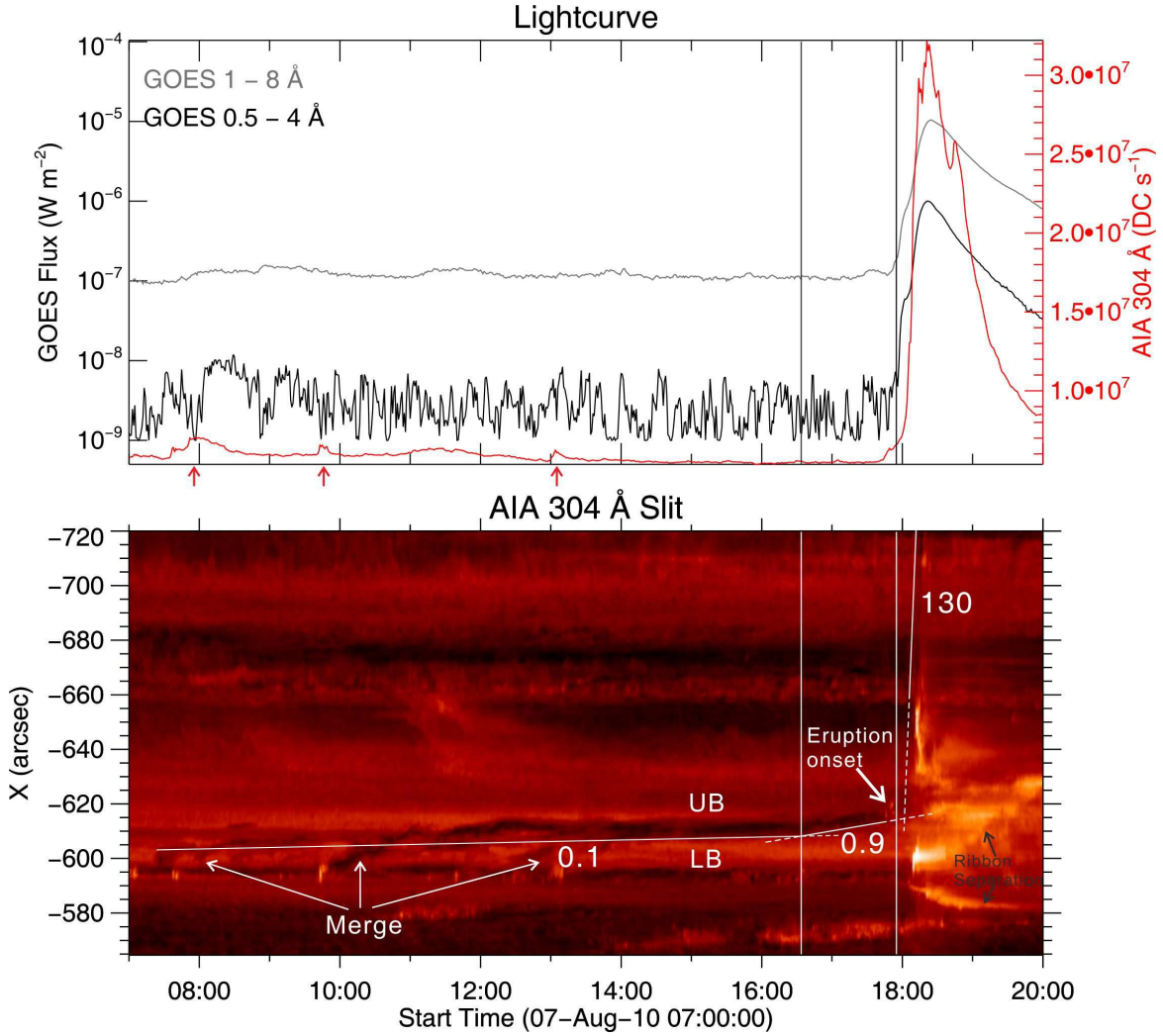


FIG. 4.— Intermittent merging process observed in AIA 304 Å. *Top panel:* GOES and AIA lightcurves. The AIA lightcurve (red) is obtained by integrating over the green box in Figure 5(a). Three bumps in the lightcurve corresponding to the heating at the start of each merging process are marked by arrows in the bottom. *Bottom panel:* a space-time diagram (stack plot) obtained from the slit displayed in the accompanying animation of AIA 304 Å images for the same time interval, with all images being registered with the first image at 07:00:10 UT. The intensities in the space-time diagram are displayed in logarithmic scale. The first two sloping lines are adjusted to the western edge of the upper branch, which is better defined than its eastern edge, and the third sloping line follows the eruptive feature, which briefly swept across the slit from 18:07 to 18:17 UT. Dashed lines are simply extensions of the solid lines which outlines the corresponding features. The implied velocities are quoted in km s^{-1} . The two vertical lines mark the crossing of the first two sloping lines and the onset of the GOES flare, respectively.

119.1'' to 124.5'' in the north-south direction (see the animation accompanying Figure 4). The intensities are summed in vertical direction, and the solar rotation and differential rotation are removed. The resulting space-time diagram is plotted in Figure 4 in the range 07:00:10 to 19:59:10 UT. Three exemplary mergers occurring within 10 hours prior to the eruption are visible. Each merger corresponds to a small bump in the light curve of the AIA 304 Å channel (top panel of Figure 4), which is obtained by integrating over a region enclosing the filament (Figure 5(a), green box). The bumps manifest the heating of the filament, due to the reconnection associated with flux transfer from the lower to the upper branch. Assuming dominantly horizontal field direction in the filament, the mass transfer implies a corresponding flux transfer.

The merging episodes cannot be associated with significant changes in the position of the branches, but they occurred in a long-lasting phase of very gradual displacement (likely gradual rise) of the upper branch, as indicated by the first of the

three sloping lines in Figure 4. The slope of the line represents a velocity of 0.1 km s^{-1} in the plane of the sky, consistent with the average rise velocity since August 5 ($\sim 0.1 \text{ km s}^{-1}$) estimated from the three-dimensional reconstruction in Section 2.3. Both the transfer of flux into the upper branch and the weakening of the overlying field by the gradual cancellation are plausible causes of the indicated very gradual rise of the branch.

Following the mergers, the upper branch appeared thicker and darker, presumably due to the mass loading effect. A few other factors could also affect the observed absorption, such as Doppler shift, change in perspective, shift of the filament structure, and condensation of coronal plasma. It is difficult to evaluate how these effects impact on filament darkness and thickness in relation to the mass loading, which is the most obvious factor.

About 1.5 hours prior to the eruption, the displacement of the upper branch accelerated slightly to reach more typical

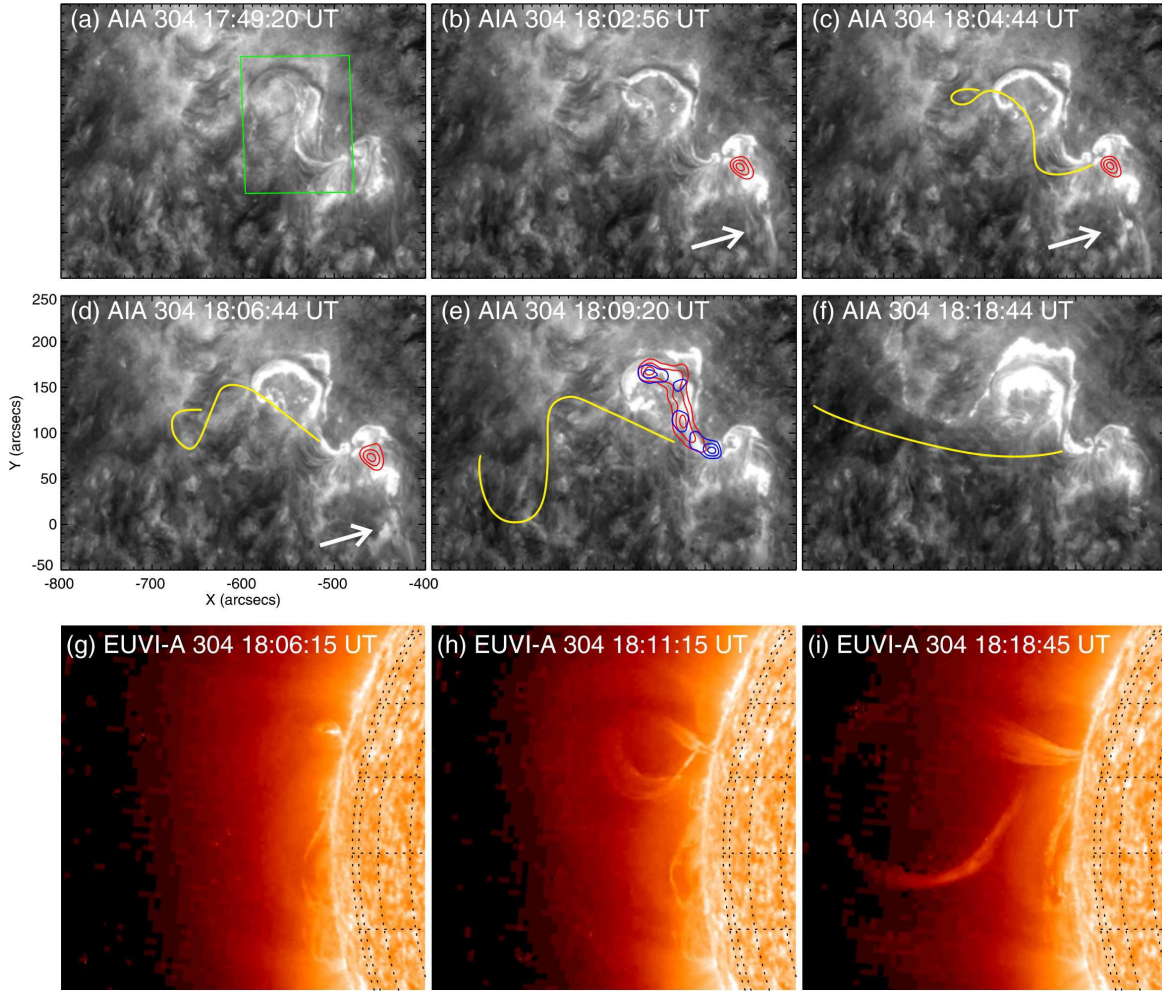


FIG. 5.— Filament eruption observed in He II 304 Å in two different viewpoints. Panels (a)–(f): snapshots of AIA 304 Å images, overlaid by contours indicating *RHESSI* emission at 3–9 keV (red) and 15–40 keV (blue), respectively. Contour levels are set at 50%, 70% and 90% of the maximum brightness of each individual image. Yellow curves highlight the upper branch of the filament which was too diffuse to be seen in static images but visible in the animation accompanying the figure; in the animation, the left panel shows an original AIA 304 Å image and the right panel shows the same image enhanced with a wavelet technique). White arrows mark the flare spray propagating along the transequatorial loops connecting to AR 11095 in the southern hemisphere. Panels (g)–(i): 304 Å images obtained by the Ahead satellite of *STEREO*. The green box in Panel (a) marks the integration area to obtain the AIA 304 Å lightcurve in Figure 4. It is slightly slanted due to differential rotation, as the box is defined in the image at 07:00:08 UT.

velocities of a slow-rise phase; the slope of the second line in Figure 4 corresponds to about 0.9 km s^{-1} . Whether this change occurred abruptly at the crossing time (16:34 UT) of the lines or gradually, and whether it was due to external influences or changing conditions in the filament, cannot be determined from the available data. No significant external influence on the filament can be discerned near this time.

Threads in the upper branch lightened up in the EUV from about 17:42 UT. The resulting mix of dark and bright structures strongly increased the visibility of the internal motions in both branches (see the animation accompanying Figure 5). At earlier times, motions directed toward the sunspot could be seen throughout the lower branch and in the southwest half of the upper branch. With the onset of the brightening, the motions in the upper branch intensified, becoming faster in the southwest half. Additionally, motions toward the other end of the branch became very visible in the northeast half (this may be a true enhancement or be due to the improved perception). The motions toward the ends of the upper branch continued into the onset phase of the eruption.

The eruption of the upper filament branch commenced

in relatively close temporal association with the soft X-ray (SXR) flare. It can be seen from Figure 4 that the brightening and acceleration of the upper branch (marked by an arrow) started slightly earlier (about 10 min) than the onset of the *GOES*-class M1.0 flare at about 17:55 UT. Due to the acceleration, the crossing time of the second and third sloping lines slightly lagged (about 7 min) behind the onset of flare. Within about two minutes, also a flare spray was ejected from the vicinity of the sunspot, but into a different direction (Figure 5). The flare spray propagated along the transequatorial loops connecting with AR 11095 in the southern hemisphere (see also Figure 1). The lower branch of the filament, on the other hand, obviously remained stable at its original location, flanked by a pair of conjugate flare ribbons in 304 Å separating from each other (Figure 5, see also Vemareddy et al. 2011 for a study of the ribbon separation in relation to the filament eruption). The eruption evolved into a fast CME detected by the *SOHO*/LASCO and *STEREO*/COR coronagraphs.

The upper filament branch experienced a dramatic change of shape in the course of its eruption. Originally, it had a strong reverse S shape following the PIL (Figures 3 and 5).

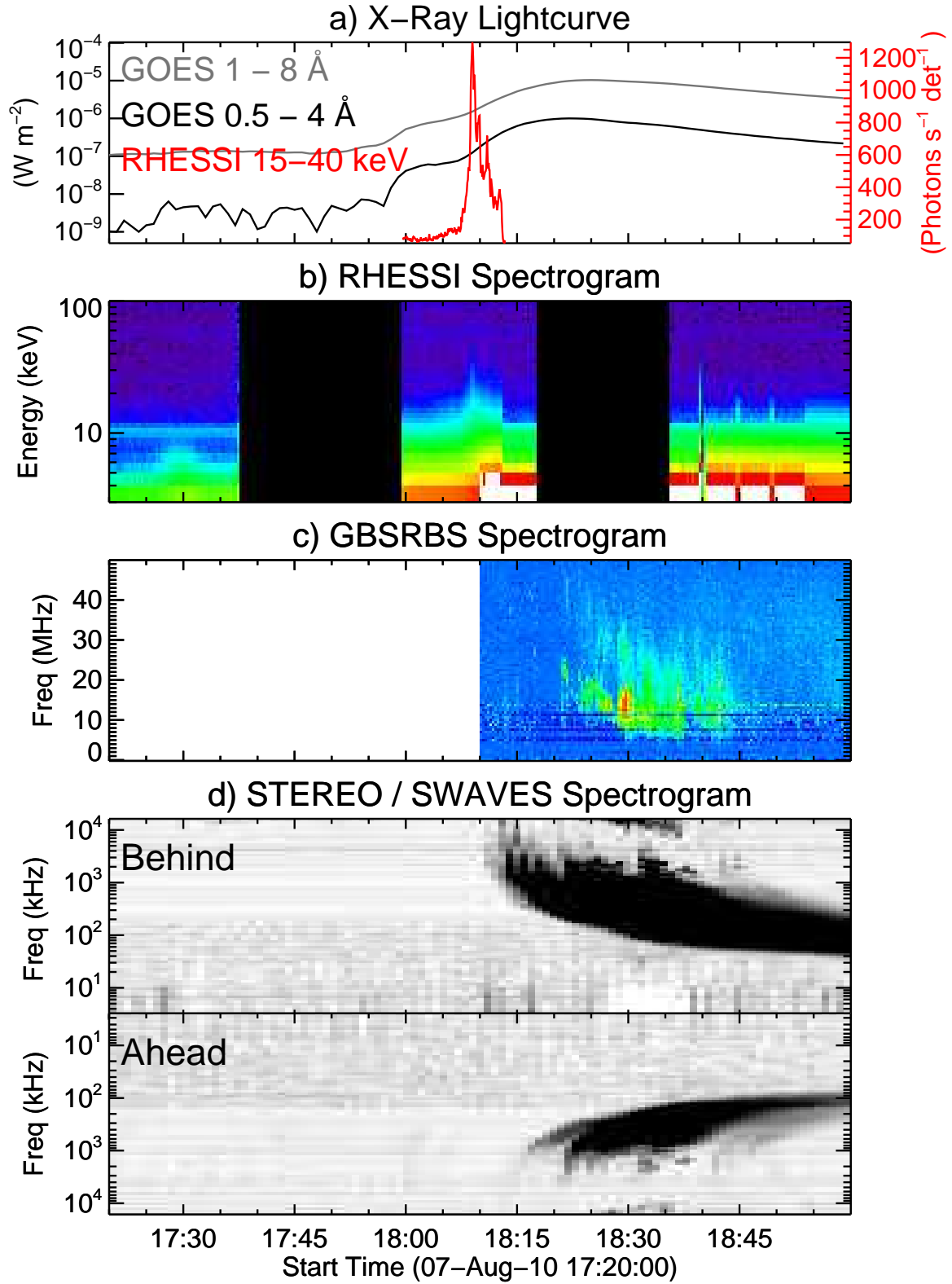


FIG. 6.— Time evolution of the filament eruption in X-rays and radio.

The AIA images in Figure 5 first indicate a straightening of the branch (Panel (c)), followed by a strong writhing into a forward S shape (Panels (d)–(e)). With yellow curves, we highlight the shape of the branch, which was too diffuse to be clearly seen in static images, but is visible in the animation of these images accompanying Figure 5. Both the reverse S shape of the low-lying filament branches and the forward S shape of the erupted, high arching upper branch are signatures of left-handed writhe (Török et al. 2010), indicating left-handed chirality for this dextral filament.

These considerations are supported by the *STEREO* data. In the *STEREO*-A 304 Å images in which the upper branch of the filament was above the east limb from 18:06 UT, a leg-crossing loop configuration developed (Figure 5(g)–(i)), indicative of strong writhing. By examining the animation of AIA 304 Å images, one can see that the filament leg that was fixed at the sunspot penumbra was more perceptible than the other leg which became too tenuous to be seen by 18:05 UT. Assuming a similar visibility for the corresponding *STEREO*-A images in the same wavelength, we identify the filament leg that was apparently attached to the surface in the *STEREO*-A view (Figure 5(h)–(i)) with the leg fixed at the sunspot penumbra in the earth view (Figure 5(a)–(f)). Since this footpoint is closer to the observer, the filament traces a left-handed helical curve, consistent with the left-handed writhe inferred from the counterclockwise rotation of the filament’s upper section in the AIA images (Figure 5(c)–(e)).

2.5. Associated Flare

X-ray flaring activity associated with the eruption commenced as a microflare at 17:30 UT, detected by *RHESSI* in the energy range ≈ 3 –9 keV (Figure 6(b)). In the *GOES* soft X-ray flux, the signal was very weak, barely above the background noise (Figure 6(a)). *RHESSI* images at 3–9 keV show a compact source located to the west of the sunspot. The source location and morphology was almost identical to the early phase of the *GOES*-class M1.0 flare starting at about 17:56 UT (Figure 5(b)–(d)), suggesting that the magnetic configuration stayed largely unchanged in this interval. No specific change in the filament can be associated with the microflare. It appears that this tiny event did not play any significant role in the evolution toward the eruption.

The spatial and spectral evolution of the M1 flare is shown in Figures 7 and 8, respectively. Throughout the flare interval, the spatially integrated spectra can be well fitted by an isothermal, exponential component below about 10 keV (red line) and a nonthermal, power-law component above about 15 keV (blue line) plus a narrow Gaussian component emulating the iron-line complex at 6.7 keV (green line). Toward the flare peak, the power-law section hardened significantly, and the flare morphology underwent a drastic change as the upper branch of the filament rose and writhed. Until 18:08 UT, the compact source to the west of the sunspot was still visible, but new emission began to develop to the east of the sunspot from 18:06 UT, whose shape roughly followed the curved filament. At the peak of the nonthermal emission at about 18:09 UT (Figure 6(a)), a sigmoidal HXR source was fully developed (Figure 7(h) and (i)), outshining the compact source to the west of the sunspot.

In the dynamic spectrograms obtained by the Green Bank Solar Radio Burst Spectrometer (GBSRBS⁷) on the ground

(Figure 6(c)) and the WAVES instrument onboard *STEREO* (Bougeret et al. 2008) (Figure 6(d)), one can see a fast-drift burst (type III) starting at about 08:12 UT near 35 MHz, indicating the escape of some nonthermal electrons along open field lines, presumably due to the interaction of the filament field with the surrounding field. One can also see a slow-drift (type II) burst commencing at about 18:20 UT near 50 MHz, which reveals the formation of a large-scale coronal shock by the fast CME.

2.6. Coronal HXR Sigmoid

The HXR nonthermal emission at 15–40 keV was composed of four kernels, *K1*–*K4* (Figure 9(a)), at the flare peak. Overall it took a reverse S-shape, and *K1*–*K3* were co-spatial with the thermal source (3–9 keV) that possessed a continuous, reverse S-shape passing over the PIL. This thermal sigmoidal source was roughly projected to the gap between the two filament branches in the AIA 304 Å image (Figure 9(a)), and was co-spatial with a hot ridge in the temperature map (Figure 9(b)) which is obtained with the differential emission measure (DEM) method utilizing the six AIA coronal wavelengths (131, 171, 193, 211, 335, and 94 Å; Aschwanden & Boerner 2011). The temperature of this hot ridge is consistent with the isothermal temperature of the SXR emission derived from spectral fitting (~ 12 MK; Figure 8), confirming that the flaring plasma was observed by both *RHESSI* and AIA. Thermal sources are usually coronal sources, not footpoint sources. The continuous structure, passing over the PIL, clearly favors a coronal source in the present event as well. The hot ridge must show plasma in the flare current sheet above the arcade of flare loops or the tops of the flare loops which are known to often have the highest brightness in the arcade.

From the above observations, we conclude that the sigmoid featured by SXR emission was of coronal origin. But were the nonthermal kernels, *K1*–*K4*, coronal or footpoint sources? First of all, we believe that these kernels are unlikely “ghost” images due to the pulse pileup effect (Smith et al. 2002; Hurford et al. 2002), as the fractional livetime is relatively high (87.96% at the peak of the nonthermal emission) and the countrate is relatively low (the peak countrate at 12–25 keV is $\sim 200 \text{ s}^{-1} \text{ det}^{-1}$ with no attenuators in front of the detectors). The spatially resolved spectra of *K3* and *K4* (Figure 11) were significantly harder than the other two kernels, making these the strongest candidates for footpoint sources. The source *K4* coincided with the southern end of the western, negative-polarity ribbon *R_W* (Figures 9(c) and 10), and it was spatially distinct with both the SXR source and the EUV hot ridge (Figure 9(b)), hence it was very likely a footpoint source. The sources *K1*–*K3* had projected locations on the positive-polarity side of the PIL. While the stronger source *K1* fell on the eastern, positive-polarity ribbon *R_E*, the centroids of *K2* and *K3* were clearly displaced from the ribbon. (Note that *R_E* was shorter, ending near *K3*, while *R_W* ended at *K4*.) Moreover, both UV ribbons were formed as early as 18:04 UT, before the HXR sigmoid appeared (Figure 10). This is in contrast to previously reported cases, in which UV bright kernels tended to be both co-spatial and co-temporal with HXR footpoints (e.g., Warren & Warshall 2001; Liu et al. 2007a; Qiu et al. 2010), although the latter are often more compact. This timing, the spatial association of *K2* and *K3* with the SXR source and their displacement from the UV ribbon are all naturally explained if *K2* and *K3* were coronal sources.

⁷ <http://gsbrbs.nrao.edu/>

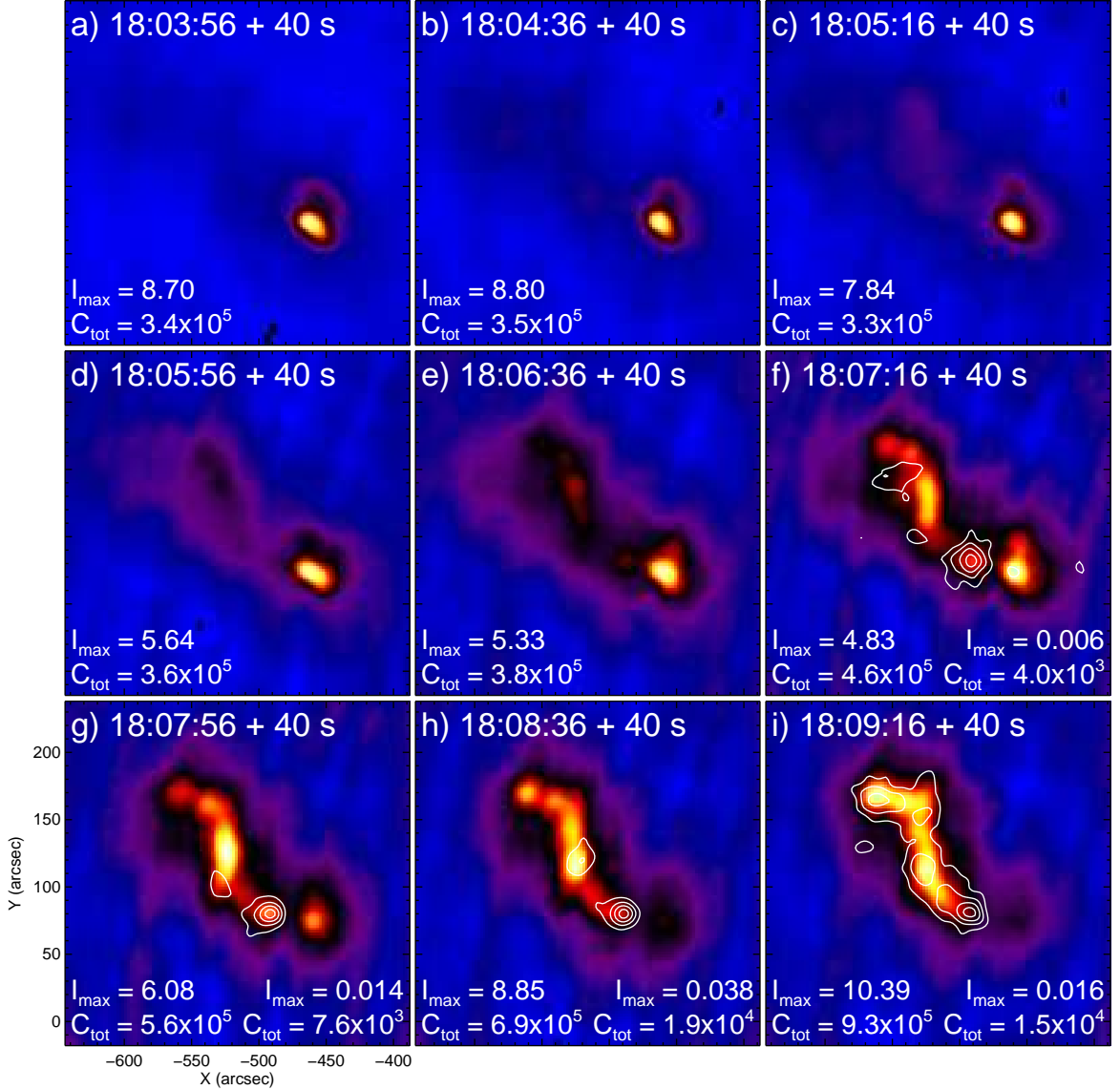


FIG. 7.— Evolution of flare morphology in HXR. The figure shows a series of *RHESSI* CLEAN images at 3–9 keV, overlaid by contours at 50%, 70% and 90% of the maximum brightness, I_{\max} (photons $\text{cm}^{-2} \text{s}^{-1} \text{arcsec}^{-2}$) of each image obtained for the same time interval at 15–40 keV. I_{\max} is given in the bottom left (right) of each panel for the 3–9 (15–40) keV energy ranges; also quoted is C_{tot} , the total counts accumulated by Detectors 3–8.

The nature of kernel *K1* is less clear: its location is consistent with a footpoint source (although not inconsistent with a coronal source falling on the ribbon only in projection), while its soft spectrum, similar to *K2* (Figure 11), indicates a coronal source. Overall, the HXR sigmoid observed here is at least partly of coronal origin, different from that reported by Ji et al. (2008), which appeared in a typical flare morphology with two conjugate footpoints and a looptop source.

3. INTERPRETATION

3.1. Filament Chirality and Magnetic Configuration

The writhing motion and the consequent formation of the left-handed kink clearly indicate that the upper branch of the filament was embedded in a left-handed flux rope. Thus, the inverse polarity configuration is indicated for this branch. The helicity sign of the lower branch can be inferred from its magnetic connections at the ends, which were the same as for the upper branch, and from its interaction with the upper branch. The MHD simulations by Linton et al. (2001) showed that

two parallel flux tubes with the same sign of helicity tend to merge while those with the opposite sign of helicity tend to bounce off each other. Thus, left-handed helicity is indicated for the lower branch as well.

However, the lower branch could be either embedded in a flux rope with the inverse polarity configuration (Figure 12(a)) or in a sheared arcade (Figure 12(b)) with the normal polarity configuration. The latter case simply corresponds to a flux rope configuration bounded below by an X-type structure, i.e., in general a hyperbolic flux tube (HFT; e.g., Titov et al. 2002). It is well known that this configuration admits of both stable and unstable states for the flux rope (while the arcade below does not erupt): the helical kink mode and the torus instability have been demonstrated to occur if the flux rope's twist or height exceed a threshold (e.g., Török et al. 2004; Török & Kliem 2007). The consideration of the former case in Paper II shows that it likewise admits of both stable and unstable states for the upper flux rope, with the lower flux rope being stable (in addition to states with both ropes being unsta-

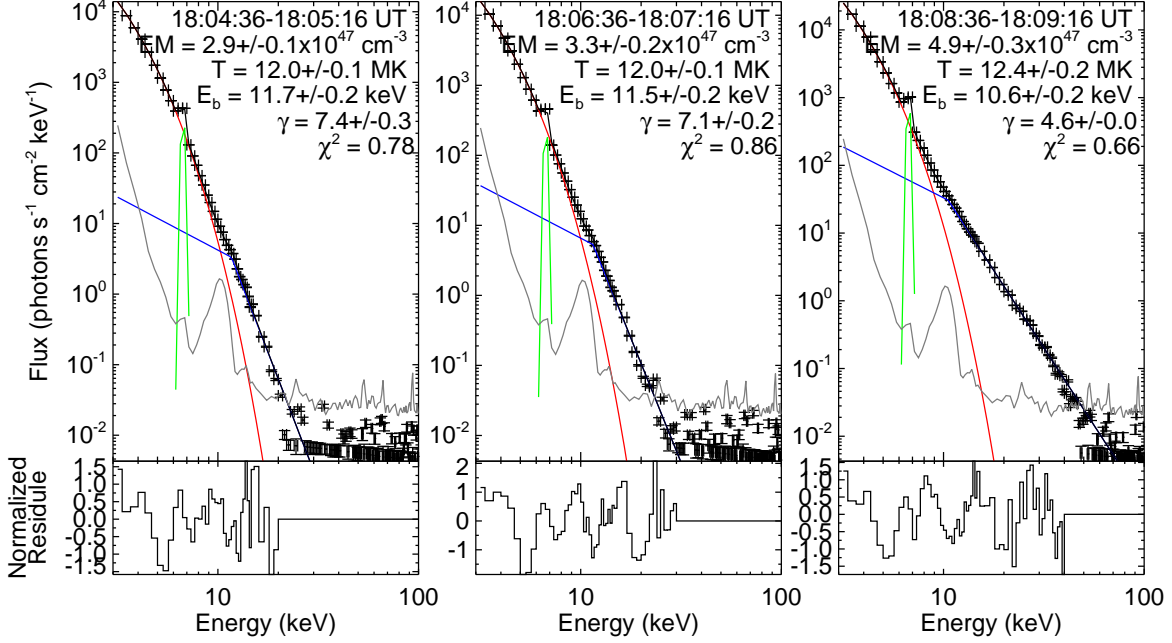


FIG. 8.— *RHESSI* spatially integrated, background-subtracted spectra and the corresponding spectral fits. The three time intervals correspond to the three panels in the middle column of Figure 7. The red line indicates an optically thin thermal bremsstrahlung radiation function, the blue line a broken power-law function, the green line a Gaussian function, and the grey line the background. The fitting parameters are shown in each panel, including emission measure (EM), temperature (T), break energy of the broken power-law function (E_b), spectral index (γ) above the break energy, and Chi-square (χ^2) of each fitting, assuming a system uncertainty of 5%. The spectral index below the break energy is fixed at 1.5. The maximum energy to fit is chosen automatically by the software based on the spectral values with respect to the background. Fitting residuals normalized to the 1σ uncertainty of the measured flux are shown at the bottom. Detectors 1, 4, and 6 are used.

ble). Consequently, both configurations sketched in Figure 12 represent plausible models for the observed double-decker filament.

3.2. Formation Mechanism

A question naturally arises as to how a double-decker configuration containing two flux ropes in equilibrium can form. We provide two possible scenarios as follows.

- The lower branch emerges from below the photosphere after the upper branch has formed above the PIL. This is motivated by the recent *Hinode* observation which suggests that a flux rope can emerge under a pre-existing filament (Okamoto et al. 2008). In this particular observation, the upper and lower flux systems appeared to merge within a couple of hours right after the emergence of the lower flux system (Okamoto et al. 2009). Such merging may be delayed or inhibited if the upper flux system is elevated to substantial heights or if the ambient field between the flux systems is very strong (see Paper II for the latter case).
- Both branches originally belong to a single flux rope or flux bundle and are separated later. This is motivated by the “partial eruption” scenario proposed by Gilbert et al. (2001), in which the reconnection within a stretched flux rope splits it into two ropes with the same handedness. However, it is unclear whether the two ropes can remain in equilibrium for an extended period of time (a few days), since in previous simulations (e.g., Gibson & Fan 2006b) and observations (e.g., Gilbert et al. 2001; Liu et al. 2007c; Gilbert et al. 2007; Tripathi et al. 2009; Régnier et al. 2011) the splitting often occurs during the eruption, or, in some cases, shortly before the eruption (e.g., Contarino et al. 2003; Guo et al. 2010). See Paper II for a new simulation addressing this problem.

We suggest that a double-decker configuration is not a unique occurrence, since it is possible for either branch to be void of filament material so that only a single-branch filament is visible. In particular, it is sometimes observed that a filament survives the eruption directly above it (e.g., Pevtsov 2002; Liu et al. 2007b,c, 2010). This could be similar to the eruption studied here except that the upper branch is not traced by filament material. As the upper branch rises, reconnection occurs between the oppositely-directed legs of the overlying field which recloses between the two branches, so that the lower branch is confined by the newly reconnected field (similar to the middle panel of Figure 3 in Gilbert et al. 2001).

3.3. Flux Transfer

The transfer of material from the lower to the upper filament branch implies a corresponding transfer of flux if the field in the filament has a dominantly horizontal direction, which is the standard configuration at least for active-region filaments. Such transfer of flux through the HFT between the filament branches is different from a conventional reconnection process at the HFT (e.g., tether-cutting reconnection), which would exchange flux in both branches with the ambient flux. Thus it must be due to upward Lorentz forces of the current-carrying flux in the lower branch which enforce part of this flux to rise even through the HFT. Such a process is conceivable if part of the flux in the lower branch is particularly stressed (sheared or twisted) by appropriate photospheric changes in its footpoint areas. It is also natural to expect that such flux rearrangement is accompanied by reconnection between the flux of the lower branch and that of the upper branch. We conclude that the transfer of flux as indicated by the observed mass transfer must involve a transfer of current from the lower to the upper filament branch. This will

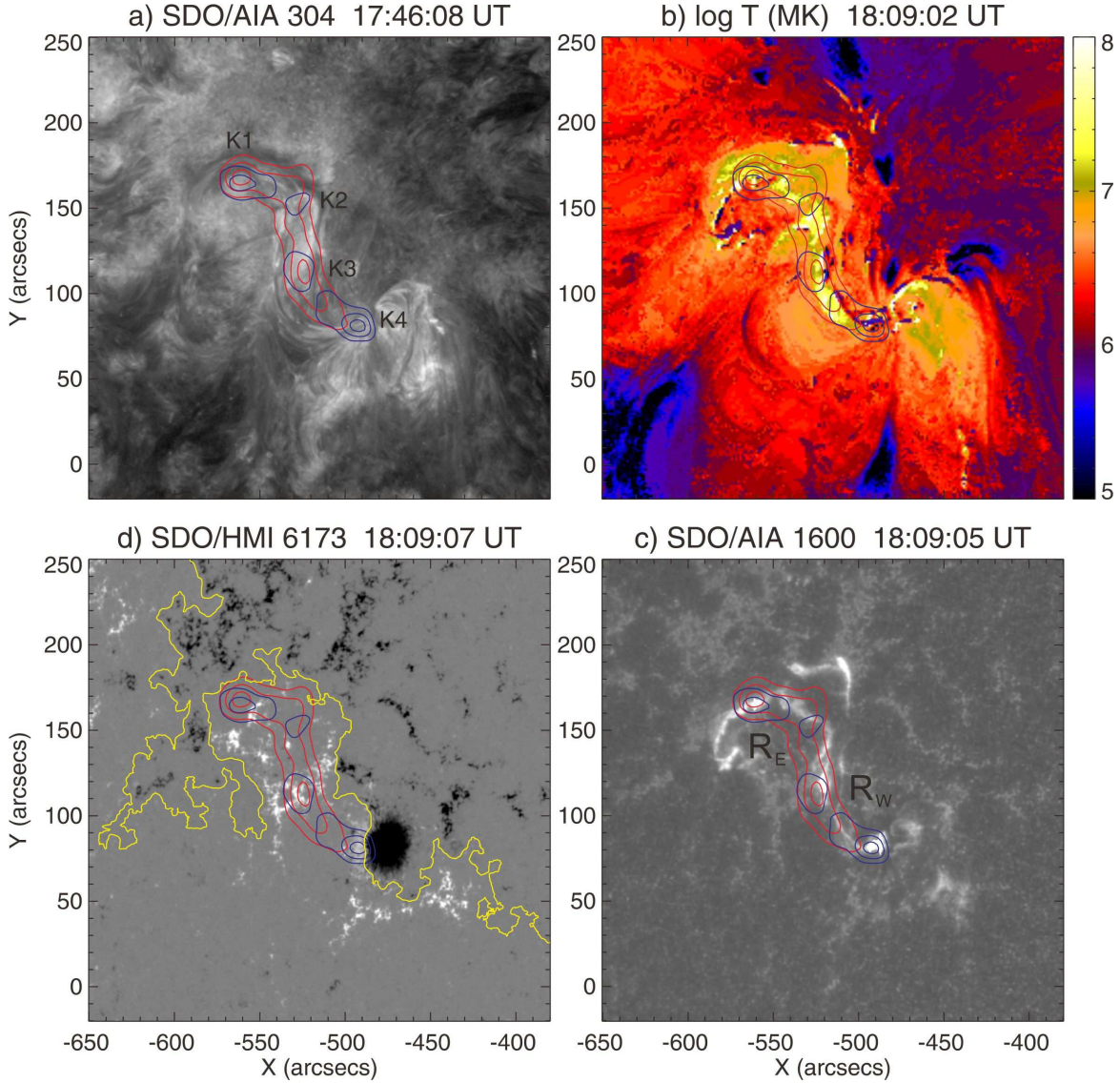


FIG. 9.— Sigmoidal HXR source in relation to (a) the double-decker filament, (b) flaring loops in the corona, (c) flare ribbons in the chromosphere, and (d) photospheric line-of-sight magnetic field. Panel (b) is a temperature map obtained with the DEM method using six AIA coronal channels. Red and blue contours show the 3–9 and 15–40 keV emission, respectively, integrated over 18:09:16–18:09:56 UT.

be further considered in the modeling of the partial eruption in Paper II.

3.4. Eruption Mechanism

3.4.1. Role of the Helical Kink Instability

The pronounced writhing of the upper filament branch into a projected forward S shape in the course of its rise is an indication for the occurrence of the helical kink instability. However, since the filament had a low-lying, reverse S shape prior to the eruption, it must have temporarily straightened out during the initial rise before it could adopt the high-arching, forward S shape. Both a low-lying reverse S shaped structure and a high-arching forward S shaped structure have negative (left-handed) writhe, while a straight loop (lying in a plane) has no writhe (Török et al. 2010). Therefore, the straightening implies a reduction of writhe, excluding the helical kink instability as the trigger of the eruption. This is because the helical kink which transforms twist into writhe is supposed to increase the writhe. The only exception is an opposite sign

of the initial twist and writhe, which would be a very unusual case and is in no way supported by the data of the considered event, which all indicate left-handed helicity.

As has also been noted in Török et al. (2010), the initial increase of the flux rope twist by the transformation of writhe helicity supports the occurrence of the helical kink in the further evolution. Part of the acquired twist would thus be transformed back into left-handed writhe. Inferring the occurrence of the instability from an observed writhing (helical kinking) alone is often not conclusive, however, since a writhing of the same sign is given to a rising flux rope by the shear component of the ambient field (Isenberg & Forbes 2007). This component is usually present and acts quite efficiently (Kliem et al. 2012a). In AR 11093 it must have been rather strong because the main polarities were situated near the ends of the filament. In order to infer the helical kink unambiguously, one needs to find a super-critical amount of twist (through observation of highly twisted substructure, magnetic field extrapolation, or a parametric study as in Kliem et al. 2012a) or features incompatible with a writhing driven (nearly) exclusively by the

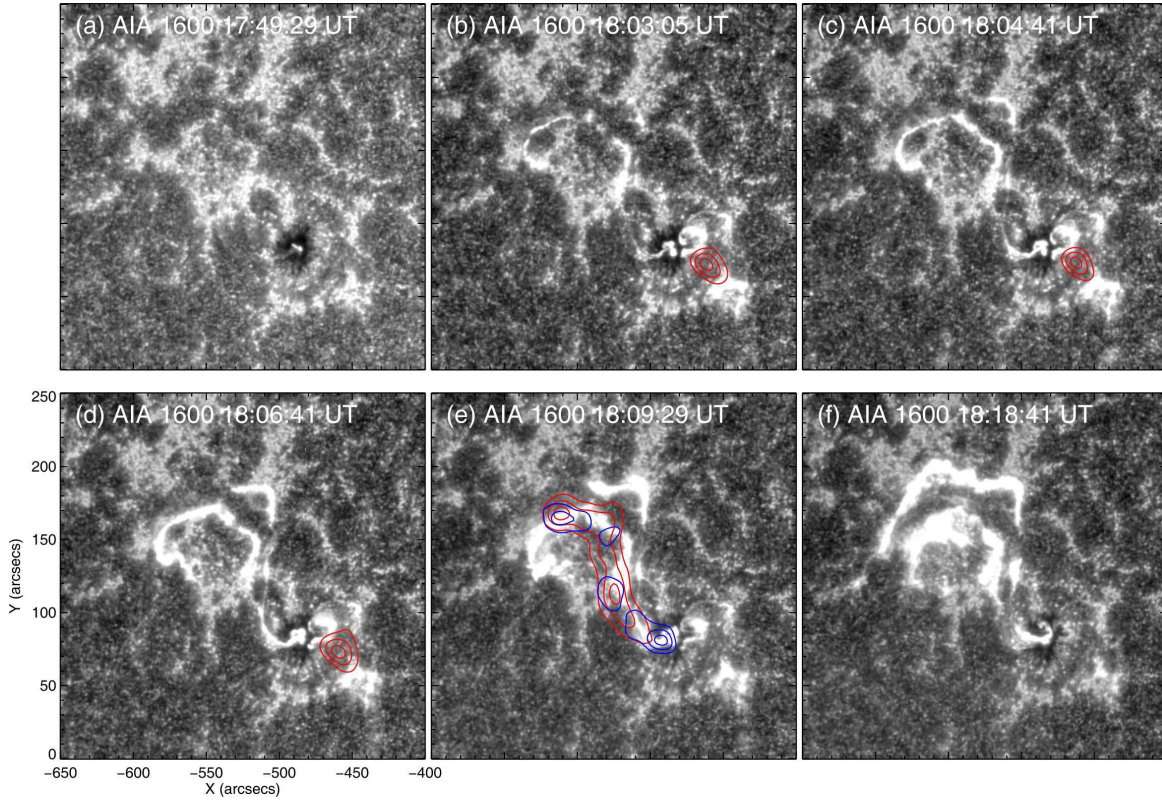


FIG. 10.— UV flare ribbons in relation to HXR emission represented by contours (same as in Figure 5).

shear field. The latter—approaching flux rope legs, apex rotation considerably exceeding 90 degrees, or more than one helical turn—were justified in Kliem et al. (2012a).

In the present case, we find an indication against a purely shear field-driven writhing from the filament shape in the *SDO* images in Figure 5(d)–(e). The filament exhibits two strong and localized bends in this phase, which, at the given oblique perspective, indicate an apex rotation exceeding 90 degrees (with respect to the line connecting the footpoints) by a considerable amount. Projection effects can easily produce such a bend on one side of a gently writhed loop with $\lesssim 90$ degrees apex rotation. However, the other leg would then appear quite straight. Two strong and localized bends are seen from many perspectives if the apex rotation clearly exceeds 90 degrees. Such a strong rotation is not expected to result from the shear field mechanism alone because the shear field causes the flux rope legs to lean to the side in opposite direction perpendicular to its own direction. If there were no further effect, the resulting rotation would always stay below 90 degrees. In fact, there is an additional contribution to the rotation from the relaxation of the twist in a rising force-free flux rope even if the twist is insufficient to trigger the helical kink. Kliem et al. (2012a) have found that this contribution is about 40 degrees if the shear field is very small, and it should be smaller for larger shear field because the shear field-driven rotation then has a share in reducing the twist. Hence, a total rotation of ≈ 130 degrees or more represents an indication for the occurrence of the helical kink instability. The two strong bends in Figure 5(d)–(e) are consistent with a rotation of this magnitude. The alignment of the filament section between the bends with the solar-y axis in Figure 5(e) is suggestive of a rotation beyond the meridional plane, since the height of the structure is initially still increasing if one goes south-

ward from the northern bend (compare the *STEREO* image in Figure 5(h)). If this section of the filament were lying in the meridional plane, then it would run slightly southeastwards in the plane of the sky for *SDO*. This suggests a rotation even slightly exceeding 135 degrees with respect to the diagonal line between the footpoints of the filament, which is an indication that the helical kink instability did occur in the main phase of the eruption.

3.4.2. Flux Imbalance and Torus Instability

Which other mechanism could have triggered this event? We suggest that it was a loss of equilibrium caused by flux imbalance or by the torus instability. Both mechanisms, which may actually be closely related, are supported by the main characteristics of the gradual evolution prior to the event's onset: the transfer of flux from the lower to the upper filament branch and the slow rise of the upper branch (Figure 4).

Through parametric study of flux ropes in numerical models of erupting active regions, it has been found that the amount of axial flux in the rope, relative to the total amount of flux in the region, possesses a limiting value for the existence of stable equilibria (Bobra et al. 2008; Savcheva & van Ballegoijen 2009; Su et al. 2011). The limiting value appears to be rather small, in the $\sim (10\text{--}20)$ percent range (although compare Green et al. 2011, who presented support for a higher value for a flux rope still in the process of formation). The conjectured flux rope in the present event was lying rather high, thus likely well developed, so that the given small limiting value appears to be relevant and a rather modest amount of flux transfer to the upper branch may have led it to a point where no neighboring equilibrium was available.

The torus instability (Kliem & Török 2006; Török & Kliem 2007) sets in if a flux rope rises to a critical height at which

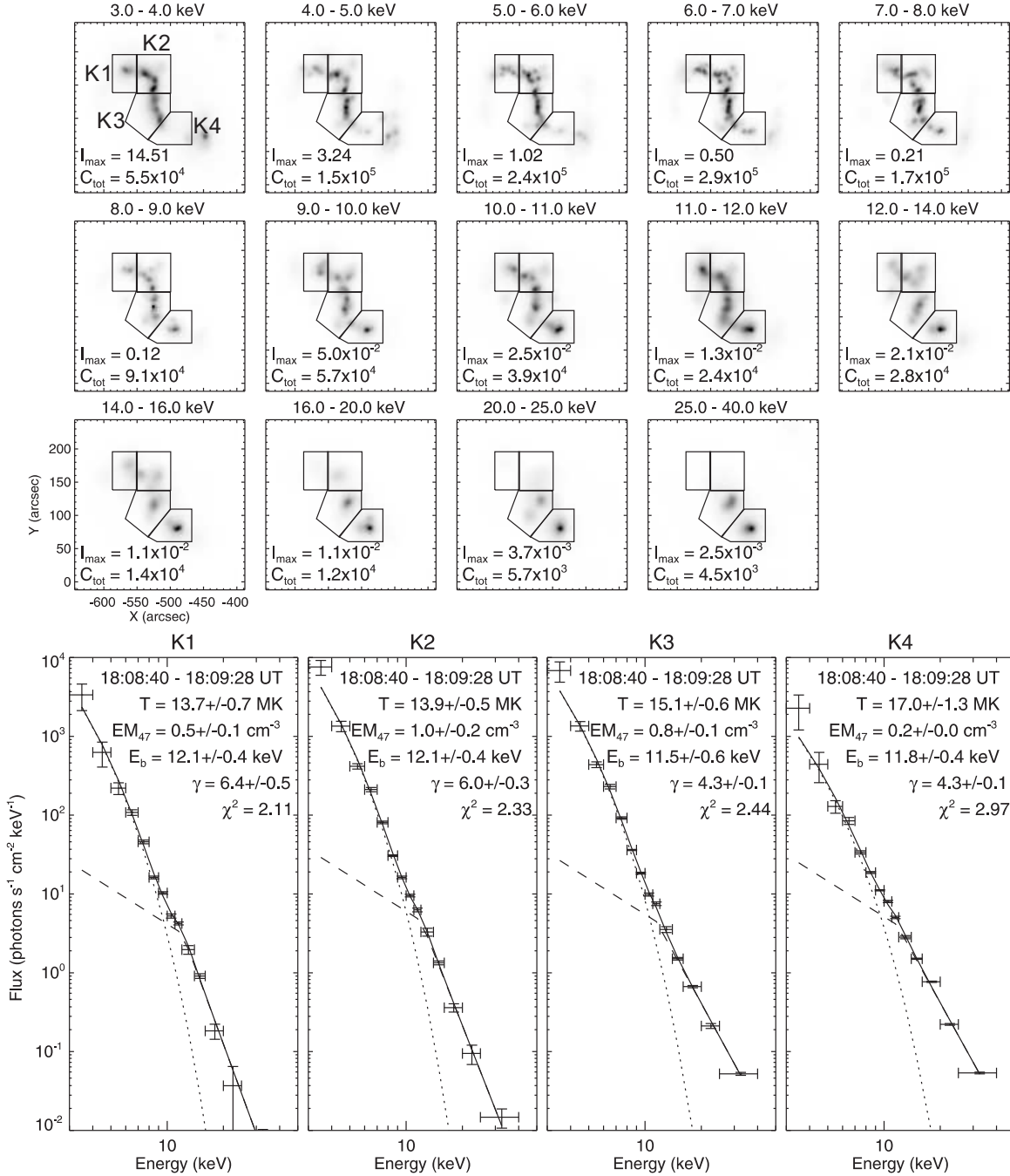


FIG. 11.— Imaging spectroscopy for a 48 s interval at the peak of the HXR burst at about 18:09 UT on 2010 August 7. Pixion images are made with detectors 2–8 in 14 energy bins from 3–40 keV. Indicated in the bottom left corner of each image are the maximum brightness, I_{\max} (photons $\text{cm}^{-2} \text{s}^{-1} \text{arcsec}^{-2}$), of each individual Pixion map, and the total counts accumulated by the detectors used, C_{tot} . The spatially resolved spectrum for each region as marked by polygons is fitted with an isothermal function (dotted line) plus a broken power-law function (dashed line) with the spectral index below the break energy being fixed at 1.5. Resultant fitting parameters, as in Figure 8, are given for each spectrum. Emission measures given as EM_{47} are to be multiplied by 10^{47} .

the overlying field declines with height at a sufficiently steep rate (Liu 2008; Aulanier et al. 2010; Olmedo & Zhang 2010; Fan 2010). Thus the observed slow rise of the upper filament branch makes this instability a potential trigger mechanism.

3.4.3. Mass (Un-) Loading

The observations in Section 2.4 show that mass is transferred from the lower to the upper branch of the filament. Mass “loading” in some form may often play a role in the final evolution of filaments toward an eruption, since their darkness

and thickness often increase in this phase (e.g., Kilper et al. 2009; Guo et al. 2010). Since this darkening is not yet fully understood, other effects, listed in Section 2.4, may be relevant in addition, or alternatively. Mass loading is very suggestive as a mechanism that helps holding down current-carrying flux, thus raising the amount of free magnetic energy that can be stored in the configuration (Low et al. 2003). A destabilizing influence of “mass unloading” may also be conjectured from the observation that the internal motions in filaments tend to amplify prior to eruption, which happened also in the

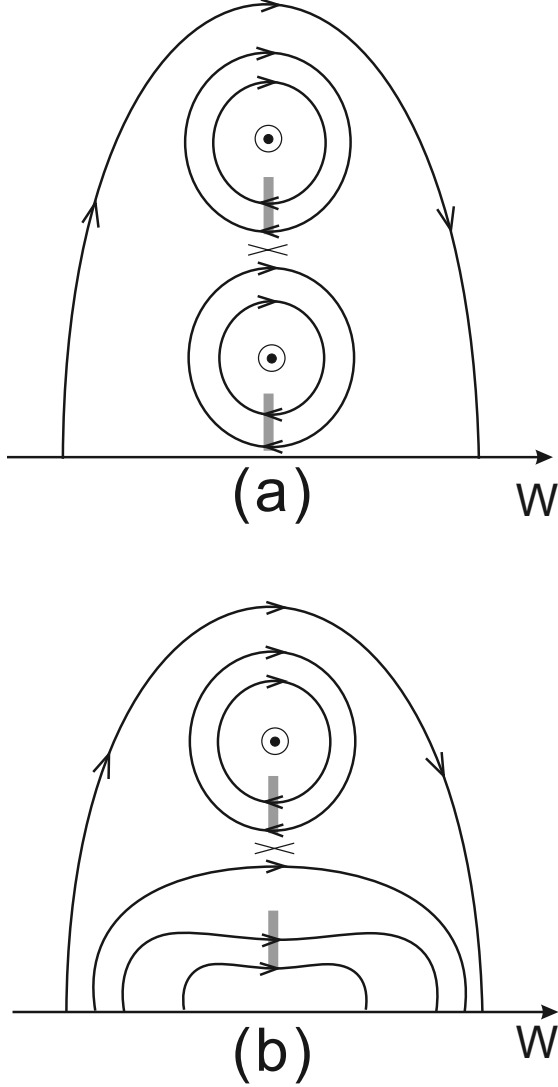


FIG. 12.— Cartoon illustrating the cross section of the two suggested double-decker filament configurations as viewed from the south. The axial field of both filament branches points out of the plane. Regions to the east (west) of the filament are associated with positive (negative) polarity. Slabs of grey color indicate the filament body.

event analyzed here. Moreover, these motions were systematically directed from the middle toward the ends of the upper branch for an extended period of time, at least ≈ 15 minutes prior to the onset of the fast rise (Section 2.4). However, a consideration of the typical gravitational and magnetic energy densities in active regions leaves mass unloading at most the role of a “final drop” in an equilibrium sequence approaching the point where the equilibrium is lost. Forbes (2000) estimates that the magnetic energy of an average active region ($B \sim 100$ Gauss) exceeds the gravitational energy by three orders of magnitude, based on a typical coronal density of 10^9 cm^{-3} . For the denser filament material, the measured values of the electron density vary greatly, ranging from 10^9 to 10^{11} cm^{-3} (Labrosse et al. 2010), due to differences among the techniques that have been used, as well as to an unknown filling factor, but the temperature is often better constrained ($T \leq 10^4 \text{ K}$). Thus, to maintain a local pressure balance, filaments must be about 100 times denser than their typical coronal surroundings ($T \simeq 10^6 \text{ K}$, $n \simeq 10^9 \text{ cm}^{-3}$). Still, the energy

density of the gravitation is at least one order of magnitude smaller than that of the magnetic field. This renders gravity largely irrelevant for the energy storage in active regions. Thus, while mass unloading of the upper filament branch may have played a minor role in the evolution toward the eruption, a role in the actual driving process can nearly certainly be excluded.

3.5. Transient HXR Sigmoid

An important structure associated with the dynamic evolution of a twisted flux rope is a sigmoidal current sheet under the rope, as revealed in various MHD simulations. The current sheet may form at a bald-patch separatrix surface (BPSS; e.g., Titov & Démoulin 1999; Magara & Longcope 2001; Gibson & Fan 2006a; Archontis et al. 2009; Fan 2010), at a hyperbolic flux tube (HFT; e.g., Titov et al. 2003; Galsgaard et al. 2003; Kliem et al. 2004), or simply in a layer of highly sheared field (Török & Kliem 2003; Aulanier et al. 2005). In each of these cases, a reverse S shaped current sheet is associated with a left-handed flux rope whose axis writhes into a forward S shape when the rope rises (Gibson & Fan 2006a; Kliem et al. 2004). The dissipation process in this current sheet and the resultant heating of plasma are suggested to be responsible for transient sigmoidal structures that brighten in soft X-rays prior to or during coronal eruptions. Our observation of the reverse S shaped HXR sigmoid underlying the left-handed kink is also consistent with these simulations.

As demonstrated in Figure 5, the coronal HXR sigmoid only formed after the upper branch of the filament had risen to relatively high altitudes above the surface. As the X-ray sigmoid is largely of coronal origin (between ~ 12 – 25 Mm ; recall Section 2.3 and see also Figure 9(a)), it is likely associated with the flare current sheet formed at the HFT. We therefore suggest that accelerated electrons trapped in this current sheet produced the HXR sigmoid.

4. SUMMARY

We investigate the pre-eruptive evolution and the partial eruption of a filament which is composed of two branches separated in height, combining *SDO*, *STEREO*, and *RHESSI* data. This is complemented by MHD modeling in Paper II. To our knowledge, such a double-decker configuration is analyzed in detail for the first time. We summarize the major results as follows.

- With stereoscopic observations from *SDO* and *STEREO-B*, we obtain the three-dimensional height information of the two filament branches. They are separated in height by about 13 Mm , and the vertical extension of the upper branch is about 10 Mm .
- The strong writhing of the upper branch into a left-handed helical kink, unambiguously determined by combining *SDO* and *STEREO-A* observations, clearly indicates the structure of a left-handed flux rope for this branch. Since the lower branch has the same magnetic connections at its ends and transfers some of its flux into the upper branch in the course of the pre-eruptive evolution, left-handed helicity is indicated also for the lower branch, hence for the dextral filament as a whole.
- This structure is compatible with two model configurations, a flux rope above a sheared magnetic arcade with dips and a double flux rope equilibrium. In either case,

the filament material in each branch can be supported against gravity by upward concave field lines, and a hyperbolic flux tube separates the branches. The first configuration is well known to possess stable and unstable states of the flux rope, with the arcade remaining stable (Titov & Démoulin 1999). Equilibria of the second type are analytically and numerically constructed in Paper II. MHD simulations demonstrate that they possess stable as well as unstable states with only the upper flux rope erupting (and also unstable states that lead to the ejection of both flux ropes).

- The pre-eruptive evolution of the filament is characterized by a slow rise of the upper branch most likely driven by the transfer of current-carrying flux from the lower to the upper branch in a sequence of partial merging episodes. Weak flux cancellation may also have contributed to the rise. These properties suggest that the eruption was triggered by reaching a point of flux imbalance between the upper branch and the ambient field (e.g., Su et al. 2011) or the threshold of the torus instability.
- The initial straightening of the erupting upper filament branch from its original reverse S-shape excludes the helical kink instability as trigger of the eruption, but it supports the occurrence of the instability in the main phase of the eruption, which is indeed indicated by the strong forward S-shape acquired in this phase.
- The main acceleration of the erupting branch commences very close in time with the impulsive phase of the associated M1-class flare. The eruption results in a

reverse S-shaped HXR sigmoid which is at least partly located in the gap between the two branches from about 12 Mm to 25 Mm above the surface. To our knowledge, this is the first time that a coronal sigmoid is clearly observed in HXRs. We suggest that electrons accelerated in the vertical (flare) current sheet under the rising filament branch produced the coronal HXR emission, in agreement with a previous model for transient sigmoids (Kliem et al. 2004).

The authors are grateful to the *SDO*, *STEREO* and *RHESSI* teams for the free access to the data and the development of the data analysis software. KSO H α data are provided through the Global H-alpha Network operated by NJIT.R. Liu acknowledges the Thousand Young Talents Program of China, NSFC grants 41131065 and 41121003, 973 key project 2011CB811403, CAS Key Research Program KZZD-EW-01-4, and the fundamental research funds for the central universities WK2080000031. R. Liu, C.L., and H.W. were supported by NASA grants NNX08-AJ23G and NNX08-AQ90G, and by NSF grants ATM-0849453 and ATM-0819662. B.K. acknowledges support by the DFG and the STFC. The contributions of T.T., V.S.T., R. Lionello, and J.A.L. were supported by NASA's HTP, LWS, and SR&T programs, and by CISM (an NSF Science and Technology Center). Computational resources were provided by NSF TACC in Austin and by NASA NAS at Ames Research Center. H.W. acknowledges travel support by Key Laboratory of Solar Activity, National Astronomical Observatories of Chinese Academy of Sciences, under grant KLSA201201.

REFERENCES

- Alexander, D., Liu, R., & Gilbert, H. R. 2006, *ApJ*, 653, 719
- Antiochos, S. K., Dahlburg, R. B., & Klimchuk, J. A. 1994, *ApJ*, 420, L41
- Antiochos, S. K., DeVore, C. R., & Klimchuk, J. A. 1999, *ApJ*, 510, 485
- Anzer, U. 1989, in *Astrophysics and Space Science Library*, Vol. 150, Dynamics and Structure of Quiescent Solar Prominences, ed. E. R. Priest, 143–166
- Archontis, V., Hood, A. W., Savcheva, A., Golub, L., & DeLuca, E. 2009, *ApJ*, 691, 1276
- Aschwanden, M. J. & Boerner, P. 2011, *ApJ*, 732, 81
- Aulanier, G. & Démoulin, P. 1998, *A&A*, 329, 1125
- Aulanier, G., Démoulin, P., van Driel-Gesztelyi, L., Mein, P., & Deforest, C. 1998, *A&A*, 335, 309
- Aulanier, G., Pariat, E., & Démoulin, P. 2005, *A&A*, 444, 961
- Aulanier, G., Török, T., Démoulin, P., & DeLuca, E. E. 2010, *ApJ*, 708, 314
- Bemporad, A., Mierla, M., & Tripathi, D. 2011, *A&A*, 531, A147
- Bobra, M. G., van Ballegoijen, A. A., & DeLuca, E. E. 2008, *ApJ*, 672, 1209
- Bommier, V., Landi Degl'Innocenti, E., Leroy, J.-L., & Sahal-Brechot, S. 1994, *Sol. Phys.*, 154, 231
- Bougeret, J. L., Goetz, K., Kaiser, M. L., et al. 2008, *Space Sci. Rev.*, 136, 487
- Chae, J. 2000, *ApJ*, 540, L115
- Chae, J., Moon, Y.-J., & Park, Y.-D. 2005, *ApJ*, 626, 574
- Cho, K.-S., Lee, J., Bong, S.-C., Kim, Y.-H., Joshi, B., & Park, Y.-D. 2009, *ApJ*, 703, 1
- Contarino, L., Romano, P., Yurchyshyn, V. B., & Zuccarello, F. 2003, *Sol. Phys.*, 216, 173
- DeVore, C. R. & Antiochos, S. K. 2000, *ApJ*, 539, 954
- Fan, Y. 2005, *ApJ*, 630, 543
- . 2010, *ApJ*, 719, 728
- Fan, Y. & Gibson, S. E. 2004, *ApJ*, 609, 1123
- Forbes, T. G. 2000, *J. Geophys. Res.*, 105, 23153
- Forbes, T. G. & Priest, E. R. 1995, *ApJ*, 446, 377
- Galsgaard, K., Titov, V. S., & Neukirch, T. 2003, *ApJ*, 595, 506
- Gibson, S. E. & Fan, Y. 2006a, *J. Geophys. Res.*, 111, A12103
- . 2006b, *ApJ*, 637, L65
- Gibson, S. E., Fan, Y., Török, T., & Kliem, B. 2006, *Space Sci. Rev.*, 124, 131
- Gilbert, H. R., Alexander, D., & Liu, R. 2007, *Sol. Phys.*, 245, 287
- Gilbert, H. R., Holzer, T. E., & Burkepile, J. T. 2001, *ApJ*, 549, 1221
- Green, L. M., Kliem, B., Török, T., van Driel-Gesztelyi, L., & Attrill, G. D. R. 2007, *Sol. Phys.*, 246, 365
- Green, L. M., Kliem, B., & Wallace, A. J. 2011, *A&A*, 526, A2
- Guo, J., Liu, Y., Zhang, H., Deng, Y., Lin, J., & Su, J. 2010, *ApJ*, 711, 1057
- Hirayama, T. 1985, *Sol. Phys.*, 100, 415
- Hood, A. W. & Priest, E. R. 1979, *Sol. Phys.*, 64, 303
- Howard, R. A., Moses, J. D., Vourlidas, A., et al. 2008, *Space Sci. Rev.*, 136, 67
- Hurford, G. J., Schmahl, E. J., Schwartz, R. A., et al. 2002, *Sol. Phys.*, 210, 61
- Inhester, B. 2006, *ArXiv Astrophysics e-prints*
- Isenberg, P. A. & Forbes, T. G. 2007, *ApJ*, 670, 1453
- Ji, H., Wang, H., Liu, C., & Dennis, B. R. 2008, *ApJ*, 680, 734
- Ji, H., Wang, H., Schmahl, E. J., Moon, Y.-J., & Jiang, Y. 2003, *ApJ*, 595, L135
- Kaiser, M. L., Kucera, T. A., Davila, J. M., St. Cyr, O. C., Guhathakurta, M., & Christian, E. 2008, *Space Sci. Rev.*, 136, 5
- Karlíčky, M. & Kliem, B. 2010, *Sol. Phys.*, 266, 71
- Karpen, J. T., Antiochos, S. K., Hohensee, M., Klimchuk, J. A., & MacNeice, P. J. 2001, *ApJ*, 553, L85
- Kilper, G., Gilbert, H., & Alexander, D. 2009, *ApJ*, 704, 522
- Kippenhahn, R. & Schlüter, A. 1957, *Zeitschrift für Astrophysik*, 43, 36
- Kliem, B., Linton, M. G., Török, T., & Karlíčky, M. 2010, *Sol. Phys.*, 266, 91
- Kliem, B., Titov, V. S., & Török, T. 2004, *A&A*, 413, L23
- Kliem, B. & Török, T. 2006, *Phys. Rev. Lett.*, 96, 255002
- Kliem, B., Török, T., & Thompson, W. T. 2012a, *Sol. Phys.*, 91
- Kliem, B., Török, T., Titov, V. S., Lionello, R., Linker, J. A., Liu, R., Liu, C., & Wang, H. 2012b, *ApJ*, submitted (Paper II)
- Kuperus, M. & Raadu, M. A. 1974, *A&A*, 31, 189
- Labrosse, N., Heinzel, P., Vial, J.-C., Kucera, T., Parenti, S., Gunár, S., Schmieder, B., & Kilper, G. 2010, *Space Sci. Rev.*, 151, 243
- Lemen, J. R., Title, A. M., Akin, D. J., et al. 2011, *Sol. Phys.*, 115
- Leroy, J. L. 1989, in *Astrophysics and Space Science Library*, Vol. 150, Dynamics and Structure of Quiescent Solar Prominences, ed. E. R. Priest, 77–113

- Li, T., Zhang, J., Zhao, H., & Yang, S. 2010, *ApJ*, 720, 144
- Lin, R. P., Dennis, B. R., Hurford, G. J., et al. 2002, *Sol. Phys.*, 210, 3
- Linton, M. G., Dahlburg, R. B., & Antiochos, S. K. 2001, *ApJ*, 553, 905
- Liu, C., Lee, J., Gary, D. E., & Wang, H. 2007a, *ApJ*, 658, L127
- Liu, C., Lee, J., Yurchyshyn, V., Deng, N., Cho, K., Karlický, M., & Wang, H. 2007b, *ApJ*, 669, 1372
- Liu, R. & Alexander, D. 2009, *ApJ*, 697, 999
- Liu, R., Alexander, D., & Gilbert, H. R. 2007c, *ApJ*, 661, 1260
- Liu, R., Liu, C., Wang, S., Deng, N., & Wang, H. 2010, *ApJ*, 725, L84
- Liu, Y. 2008, *ApJ*, 679, L151
- Low, B. C., Fong, B., & Fan, Y. 2003, *ApJ*, 594, 1060
- Low, B. C. & Hundhausen, J. R. 1995, *ApJ*, 443, 818
- Magara, T. & Longcope, D. W. 2001, *ApJ*, 559, L55
- Martin, S. F. 1998, *Sol. Phys.*, 182, 107
- Martin, S. F., Bilimoria, R., & Tracadas, P. W. 1994, in *Solar Surface Magnetism*, ed. R. J. Rutten & C. J. Schrijver, 303
- Martin, S. F. & Echols, C. R. 1994, in *Solar Surface Magnetism*, ed. R. J. Rutten & C. J. Schrijver, 339
- Moore, R. L., Sterling, A. C., Hudson, H. S., & Lemen, J. R. 2001, *ApJ*, 552, 833
- Okamoto, T. J., Tsuneta, S., Lites, B. W., Kubo, M., Yokoyama, T., Berger, T. E., Ichimoto, K., Katsukawa, Y., Nagata, S., Shibata, K., Shimizu, T., Shine, R. A., Suematsu, Y., Tarbell, T. D., & Title, A. M. 2009, *ApJ*, 697, 913
- Okamoto, T. J., Tsuneta, S., Lites, B. W., et al. 2008, *ApJ*, 673, L215
- Olmedo, O. & Zhang, J. 2010, *ApJ*, 718, 433
- Pevtsov, A. A. 2002, *Sol. Phys.*, 207, 111
- Pevtsov, A. A., Balasubramaniam, K. S., & Rogers, J. W. 2003, *ApJ*, 595, 500
- Pneuman, G. W. 1983, *Sol. Phys.*, 88, 219
- Qiu, J., Liu, W., Hill, N., & Kazachenko, M. 2010, *ApJ*, 725, 319
- Régnier, S., Walsh, R. W., & Alexander, C. E. 2011, *A&A*, 533, L1
- Romano, P., Contarino, L., & Zuccarello, F. 2003, *Sol. Phys.*, 214, 313
- Rust, D. M. 1994, *Geophys. Res. Lett.*, 21, 241
- Rust, D. M. & Kumar, A. 1994, *Sol. Phys.*, 155, 69
- . 1996, *ApJ*, 464, L199
- Rust, D. M. & LaBonte, B. J. 2005, *ApJ*, 622, L69
- Savcheva, A. & van Ballegoijen, A. 2009, *ApJ*, 703, 1766
- Seaton, D. B., Mierla, M., Berghmans, D., Zhukov, A. N., & Dolla, L. 2011, *ApJ*, 727, L10+
- Smith, D. M., Lin, R. P., Turin, P., et al. 2002, *Sol. Phys.*, 210, 33
- Su, Y., Surges, V., van Ballegoijen, A., DeLuca, E., & Golub, L. 2011, *ApJ*, 734, 53
- Thompson, W., Kliem, B., & Trk, T. 2012, *Solar Physics*, 276, 241, 10.1007/s11207-011-9868-5
- Titov, V. S. & Démoulin, P. 1999, *A&A*, 351, 707
- Titov, V. S., Galsgaard, K., & Neukirch, T. 2003, *ApJ*, 582, 1172
- Titov, V. S., Hornig, G., & Démoulin, P. 2002, *Journal of Geophysical Research (Space Physics)*, 107, 1164
- Török, T., Berger, M. A., & Kliem, B. 2010, *A&A*, 516, A49
- Török, T. & Kliem, B. 2003, *A&A*, 406, 1043
- Török, T. & Kliem, B. 2005, *ApJ*, 630, L97
- . 2007, *Astron. Nachr.*, 328, 743
- Török, T., Kliem, B., & Titov, V. S. 2004, *A&A*, 413, L27
- Tripathi, D., Kliem, B., Mason, H. E., Young, P. R., & Green, L. M. 2009, *ApJ*, 698, L27
- van Tend, W. & Kuperus, M. 1978, *Sol. Phys.*, 59, 115
- Vemareddy, P., Maurya, R. A., & Ambastha, A. 2011, *Sol. Phys.*, 413
- Warren, H. P. & Marshall, A. D. 2001, *ApJ*, 560, L87
- Wuelser, J.-P., Lemen, J. R., Tarbell, T. D., et al. 2004, in *Society of Photo-Optical Instrumentation Engineers (SPIE) Conference Series*, Vol. 5171, *Telescopes and Instrumentation for Solar Astrophysics*, ed. S. Fineschi & M. A. Gummin, 111–122
- Xu, Y., Jing, J., & Wang, H. 2010, *Sol. Phys.*, 264, 81
- Zirker, J. B., Martin, S. F., Harvey, K., & Gaizauskas, V. 1997, *Sol. Phys.*, 175, 27